DR. MARI SALMIVUORI (Orcid ID : 0000-0003-0193-0552)

Article type   : Original Article

TamPub This document has been downloaded from TamPub.uta.fi
The Institutional Repository of University of Tampere

Hyperspectral Imaging System in the Delineation of Ill-defined Basal Cell Carcinomas: A Pilot Study

M. Salmivuori MD[1,5]; N. Neittaanmäki MD, PhD[2]; I. Pölönen PhD[3]; L. Jeskanen MD[4]; E. Snellman MD, PhD[1,5]; M. Grönroos MD, PhD[1]

1) Department of Dermatology and Allergology, Päijät-Häme Social and Health Care Group, Lahti, Finland

2) Departments of Pathology and Dermatology, Institutes of Biomedicine and Clinical Sciences, Sahlgrenska Academy, University of Gothenburg, Gothenburg, Sweden

3) Faculty of Mathematical Information Technology, University of Jyväskylä, Finland

4) Department of Dermatology and Allergology, Helsinki University Central Hospital, Finland

5) Department of Dermatology, Tampere University and Tampere University Hospital, Finland

Corresponding author: Mari Salmivuori, Ihotautien poliklinikka,

Keskussairaalankatu 7, 15830 Lahti, Finland

Mobile: +358505355616, E-mail: salmivuori.mari.k@student.uta.fi

Conflict of interest: The authors declare no conflicts of interest.

ABSTRACT

Background Basal cell carcinoma (BCC) is the most common skin cancer in the
Caucasian population. Eighty percent of BCCs are located on the head and neck area.
Clinically ill-defined BCCs often represent histologically aggressive subtypes, and
they can have subtle subclinical extensions leading to recurrence and the need for re-
excisions.

Objectives The aim of this pilot study was to test the feasibility of a hyperspectral
imaging system (HIS) *in vivo* in delineating the preoperatively lateral margins of ill-
defined BCCs on the head and neck area.

Methods Ill-defined BCCs were assessed clinically with a dermatoscope, photographed, and imaged with HIS. This was followed by surgical procedures where the BCCs were excised at the clinical border and the marginal strip separately. HIS, with a 12 cm^2 field of view and fast data processing, records a hyperspectral graph for every pixel in the imaged area, thus creating a data cube. With automated computational modelling, the spectral data is converted into localisation maps showing the tumour borders. Interpretation of these maps was compared to the histologically verified tumour borders.

Results Sixteen BCCs were included. Of these cases, 10/16 were the aggressive subtype of BCC and 6/16 were nodular, superficial, or a mixed type. HIS delineated the lesions more accurately in 12/16 of the BCCs compared to the clinical evaluation (4/16 wider and 8/16 smaller by HIS). In 2/16 cases, the HIS-delineated lesion was wider without histopathological confirmation. In 2/16 cases, HIS did not detect the histopathologically confirmed subclinical extension.

Conclusions HIS has the potential to be an easy and fast aid in the preoperative delineation of ill-defined BCCs, but further adjustment and larger studies are warranted for an optimal outcome.

INTRODUCTION

Basal cell carcinoma (BCC) is a locally destructive and rarely metastasising non-melanoma skin cancer (NMSC), which comprises 40% of all cancers worldwide[1].

Eighty percent of NMSCs are BCCs[2]. The incidence of BCC is as high as the incidence of all other cancers combined, and its incidence continues to increase, also affecting ever-younger populations[3-5]. BCC is causing a remarkable burden via healthcare costs, treatment capacity, and the morbidity of affected individuals[1,2,4].

Histologically, BCCs can be classified by their morphological growth pattern into indolent (nodular and superficial) or aggressive (micronodular, morpheaform, infiltrative, and metatypical – i.e. basosquamous) types[6]. In 27–43% of cases, a combination of different patterns – i.e. a mixed histology – exists[6-8]. The histological subtype affects the clinical choice of treatment and the prognosis[6]. A high risk of recurrence is associated most importantly with aggressive growth patterns along with location in high-risk anatomic areas (nose, ears, eyes, and periocular areas), clinically unclear visualisation of the border, immunosuppression, recurrence, and perineural involvement[9]. Clinically, BCCs are classified by visual assessment as either indolent (nodular, superficial) or ill-defined (aggressive subtypes)[9]. Roughly one out of five BCCs is the histologically verified aggressive subtype[6,10]. However, the proportion might be even higher. The accuracy of a punch biopsy in the interpretation of a mixed histology is 37%[11]. Moreover, in 39.1% of aggressive BBCs, the punch biopsy fails to identify the subtype correctly compared to the following excision, and 11–14.1% of any type of BCC shows an unsuspected aggressive component in the excision compared to the preceding punch biopsy[8,11].

The incidence of BCC is highest in the most sun-exposed anatomic locations[12]. Thus 80% of BCCs – and most of the aggressive types – are located on the head and neck area[2,13], where preserving the anatomy and function plays a major role. Surgery and, if

available, Mohs micrographic surgery (MMS) with a 100% margin control is the treatment of choice for high-risk BCCs[9].

Hyperspectral imaging is based on tissue chromophores (like melanin if present, haemoglobin, proteins, and water) affecting the absorption and scattering of emitted light, thus causing, together with autofluorescence, a unique spectral graph for different biological tissues[14]. A hyperspectral imaging system (HIS) has shown potential in the preoperative delineation of lentigo maligna[15] and the detection of field-cancerised skin[16]. In this pilot study, the aim was to test the feasibility of HIS in the preoperative delineation of the lateral margins of ill-defined BCCs on the head and neck area.

MATERIALS AND METHODS

We followed the Declaration of Helsinki, and the Ethics Committee of the Tampere University Hospital District, Finland, approved our study protocol. All the recruited volunteering patients were informed orally and in writing, and they provided their written consent.

Patients

Twenty-three patients with 24 lesions were recruited prospectively between March 2014 and March 2017 at the Department of Dermatology and Allergology at the Päijät-Häme Social and Health Care Group, Lahti, Finland. The inclusion criterion was a clinically assessed primary BCC with a visually ill-defined margin on the head and neck area, and which was later histologically confirmed to be a BCC. Eight BCCs

from seven patients were excluded: six because these were not treated according to the study protocol (3 represented only the superficial subtype and were treated with cryosurgery, and 3 were operated on without a separate circumferential marginal strip). Furthermore, one patient was excluded due to the imaging artefacts and one due to discrepancy in the histopathological statement (subclinical extension shown only in the preoperative biopsies and not in the separate margin strip).

Thus, 16 patients (7 female and 9 male) with 16 lesions completed the study. The mean age of the patients was 77 years (range 59–91 years). Five patients displayed anamnestic skin phototype I, nine patients displayed skin phototype II, and two patients displayed skin phototype III. Thirteen patients had a previous history of skin malignancy or its precursor, and seven of them had multiple conditions (basal cell carcinoma n=12, actinic keratosis n=8, and melanoma n=2). None of the patients had received cytostatics or radiotherapy in the study areas or received phototherapy for any skin condition. One patient had received immunosuppressive treatments.

Imaging processes

All the lesions were initially evaluated clinically and with a dermatoscope (Dermlite® 3GenCA, USA). They were photographed native with a digital camera (Canon Ixus 115 HS, 12.1 megapixel or Canon Ixus 130, 14.1 megapixel) and with the dermatoscope linked to the digital camera. The hyperspectral imaging process was performed initially without drawing the clinically assessed tumour border, and then after marking the clinical borders on the skin. The prototype of HIS is described more detailed elsewhere [15]. (In short, the VTT FPI VIS-VNIR Spectral Camera uses visible-to-near infrared light – i.e. wavelengths 500–900 nm based on a Fabry-Perot

interferometer – which enables the use of tuneable waveband selection. It has a large, 12 cm^2 field of view (FOV) with a spatial resolution of 6,400 pixels/cm^2, where one pixel is approx. 125 µm, and an imaging depth of approx. 2 mm.) [15] The hyperspectral imaging took only seconds to capture the hyperspectral data cube, which thereafter was analysed computationally in 5–10 minutes.

Data analysis

The hyperspectral data cube is a three-dimensional data cube, where the x-axis and y-axis are the dimensions on the skin surface, and the z-axis is the 70 layered hyperspectral images, where every layer is imaged on a narrow waveband. Every pixel on the skin's surface has a unique hyperspectral graph – i.e. an end-member – from which the abundance maps are calculated based on mathematical modelling (see *Fig.1*).

In this pilot study, we used mathematical modelling of linear mixture, as used in our previous studies[15,16]. These abundance maps were interpreted on site by the test-readers (M.S., M.G., I.P. and N.N.). Additionally, we developed three diverse enhanced mathematical models to create more sensitive ways to characterise the visually ill-defined margins of BCCs. Finally, the mathematical models used for the results were 1) an inversion of linear mixture model using iterative Vertex Component Analysis – i.e. the linear mixture (the one used on site), 2) an inversion of linear mixture model from the estimated single scattering albedo (SSA) using iterative Vertex Component Analysis – i.e. the linear mixture with SSA, 3) a closed form chromophore-specific approximation for the estimated SSA – i.e. chromophore specific with SSA, and 4) a modified standard normal variate correction algorithm – i.e. a standard variate. All abundance maps from these four models were interpreted

by the same test-readers. A summarised technical and mathematical presentation of the imaging system used, the algorithms, and simulated results are presented in the supplementary material, *S1*.

Each of the mathematical models used has advantages and disadvantages. The standard variate model is quite sensitive to all changes in spectra that differ from the mean spectra of the imaged area. When there is either a lot of normal skin or an ill-defined BCC, the standard variate model will distinguish the areas well. The linear mixture and linear mixture with SSA both capture changes in the concentration of skin chromophores. The chromophore specific with SSA is sensitive to skin scattering and absorption. The results from calculations with the linear mixture, the linear mixture with SSA, and the chromophore specific with SSA models can be used to simulate an imaged spectral cube. The simulated cube is a characterisation of the originally acquired image presented in the form of an abundance map for interpretation.

Surgical procedures and the histopathological sampling

After the imaging and analysis processes, and if the patient did not have an appointment for an operation on the same day, we took biopsies from the lesions and the areas where the HIS imaging indicated the BCC may be spreading. For all cases, we used a special operation technique to verify whether a subclinical extension was detected by HIS (see *Fig.1*). This included an initial excision of the tumour from the clinically and dermatoscopically detected border followed by a separately operated 2 mm circumferential marginal strip, both with orientation marks. The circumferential strip allowed us to evaluate whether there was a subclinical extension in the marginal

area. If a free margin was found in the separately excised tumour specimen, this allowed us to evaluate if the BCC was smaller than the clinical evaluation with dermatoscopy. All the samples were orientated, fixed in 10% formalin, embedded in paraffin, and cut into 3 μm thick slices, which were stained with haematoxylin and eosin and, if necessary, with CK-PAN staining for the evaluation of perineural involvement. The tumour specimens were sectioned using the normal ''bread-loaf'' technique. The circumferential strips were sectioned closely in vertical slices. The histopathological samples were analysed by an experienced dermatopathologist blinded to the HIS outcome. If the circumferential marginal strip was BCC-positive, a re-excision was performed.

RESULTS

The histopathological subtypes of the 16 included BCCs are shown in Table 1. 10/16 BCCs represented the aggressive subtype (infiltrative, infiltrative with perineural invasion, morpheaform, or micronodular features) in the final excision. In 6/16 BCCs the subtype was nodular, superficial, or a mixed histology of these two in the final excision, even though clinically all the included lesions were ill defined.

In 12/16 cases, HIS was capable of delineating the BCCs more accurately than the conventional clinical evaluation by the naked eye and with a dermatoscope. HIS-delineated lesions were wider in 4/16 of the BCCs (see *Fig.2*), and in 8/16 BCCs the lesions were delineated to be smaller than the clinical evaluation. In 2/16 cases, the HIS-delineated lesion was wider but could not be confirmed histopathologically (false positives). In 2/16 cases, HIS did not detect the histopathologically confirmed BCC in the circumferential strip (false negatives).

The results were quite similar in the four different mathematical models. If three out of four models showed similar tumour borders, those were regarded as the HIS-defined borders (see *Table 1*). However, it is still unclear which model is best for the imaging of BCC.

DISCUSSION

This study shows that HIS is feasible in detecting the borders of ill-defined BCCs, but further development work is needed to determine the optimal model for data processing.

To our knowledge, there are no earlier studies on delineating BCC margins using hyperspectral imaging technology.

Other non-invasive imaging techniques for delineating the lateral margins of BCCs include dermatoscopy, reflectance confocal microscopy (RCM), and optical coherence tomography (OCT)/high-definition optical coherence tomography (HD-OCT). In clinical practice, dermatoscopy is the most widely used for the detection of lateral margins, although its use preoperatively has not reduced the excision stages in MMS, and thus evidence of its accuracy is lacking[17]. It has been previously shown that preoperative *in vivo* use of RCM and OCT can reduce the number of excision stages in the MMS of BCCs[17].

The advantages of HIS compared to the previously studied imaging techniques in the preoperative assessment of the lateral surgical margin are the following: i) adjustable FOV up to a maximum of 12 m^2 in HIS captured and processed in 5–10 min compared to 1 cm^2 (with mosaicking) in RCM captured and processed in 2 min[18], and

6x6 mm (0.36 cm^2) in OCT, where 5x5 mm is captured and processed in 40 s[19]; ii) imaging depth of approx. 2 mm for HIS compared to 200 μm for RCM[17] and 0.2–2.5 mm for OCT, though one should note that the higher resolution is compromised by the penetration depth[19]; and iii) interpretation of HIS images is quick, easy to learn with a little experience, and does not require histological knowledge, unlike HD-OCT and RCM[17,19]. It seems that the interpretation of HIS images can be straightforward, but currently in some cases more combined information is needed from different models to conclude the interpretation, and thus further development of HIS is warranted.

Our result for 4/16 BCCs revealed that subclinical extension by HIS is quite similar to RCM in the preoperative *in vivo* assessment of the margins, as in Venturini et al.'s study, RCM found subclinical extension in 3/10 cases compared to the dermatoscopically assessed margins prior to excision[20]. OCT found the subclinical extension of BCC in 11/52 cases compared to clinical evaluation by a Mohs surgeon[21]. Wang et al. [21] had a 100% evaluation of the margins in MMS excision compared to our design with vertical sections, which is clearly a limitation in our study. Furthermore, OCT delineated the lateral margins to be smaller by 1.4 +/-1.3 mm than the clinical evaluation[21]. HIS delineated the lesion as being smaller in 8/16 cases.

In addition, high frequency ultrasound (HFUS) and fluorescence diagnosis have earlier been studied for the *in vivo* preoperative delineation of BCC. In lateral margin delineation, ultrasound has a low correlation compared to histopathology[22]. The subclinical extensions of the infiltrative and micronodular subtypes of BCC in particular are less likely to be detected by HFUS[23]. In deep margin assessment, the correlation using HFUS is intermediate[22], and in facial BCCs, there is even a good

correlation for the deep margin with histopathology[24]. HFUS has the advantage of showing underlying structures like cartilage and bone[24]. In the fluorescence diagnosis of facial BCCs, the exogenic fluorescence diagnosis has no benefit in margin assessment compared to clinical evaluation in high risk areas (though most of the BCCs were nodular in this study) [25], but in aggressive types bispectral fluorescence imaging (using autogenic and exogenic fluorescence) had some potential in delineating the margins of BCC, with a 42% agreement in lateral margin assessment compared to the histopathology of MMS[26].

A limitation of HIS is its poorer resolution compared to OCT and RCM. In this study, HIS was not used to evaluate the deep margin, which in the future might be possible with further developments given the approx. 2 mm penetration depth of HIS. However, the assessment of deep margins is also limited with RCM and HD-OCT[17]. Artefacts in HIS abundance maps can be caused by an uneven imaging surface – i.e. round and sharp forms in the imaging area, and thus one case locating on nose was excluded with low quality in the abundance maps for interpretation. With further developments of HIS, it might be possible to handle these artefacts better. Additional pathological findings (i.e. actinic keratoses, etc.) in the imaging area might also be confounding factors in the interpretation of the HIS abundance maps, and thus further development work with HIS is needed. The limitations in our pilot study design were the small number of the cases, and thus these results are preliminary. This study was not performed to distinguish BCCs from other lesions on sun-damaged skin, but rather to visualise the borders of the lesions. Thus, larger studies are warranted in the future.

Subclinical extension in aggressive BCCs can consist of cords with a thickness of a few cells[6]. Thus, in the future it would be interesting to repeat this study design by

assessing 100% of the margin and comparing the results to MMS. At the clinic where patients were recruited, MMS is not available, and thus we used the presented operation technique. Compared to MMS, in our method the separate circumferential strip was not assessed with a 100% margin control. In one true positive case, we were able to confirm subclinical extension of the marginal strip after additional histological sectioning based on the suspected subclinical extension in the HIS abundance maps. However, additional sectioning failed to reveal the subclinical extension in the two other false positive cases. It can be speculated that MMS with a 100% margin control would have revealed the histological extension in these false positive cases.

It would be interesting to investigate if HIS could be useful in MMS by reducing the number of stages by defining the margins preoperatively more accurately than the clinical evaluation, and by being faster than RCM. HIS might be also useful in reducing the number of re-excisions by more accurate preoperative assessment in intermediate- or low-risk anatomic locations, and also in high-risk areas if MMS is not available. After MMS, primary BCCs have a 4.4% recurrence and recurrent BCCs have a 3.9% recurrence in the 10-year follow-up; after traditional excision, the corresponding rates are 12.2% and 13.5%[27]. In traditional excision, the recurrence rates varies according to the width of the surgical margin, where a 2, 3, 4 or 5 mm announced negative margin has a recurrence rate of 3.96, 2.56, 1.62 and 0.39% respectively; if a positive margin is announced, the overall recurrence is 27%[28]. In the future with HIS, it might be possible to save tissues in cosmetically sensitive areas.

With the increasing incidence of BCCs, there is a need for new technologies to make the treatment of BCC less time-consuming and more cost-effective. With preliminary results of 12/16 more precisely delineated lesions and 4/16 revealed subclinical

extensions, the HIS has the potential to be a clinical aid in treatment of ill-defined

BCCs in the cosmetically sensitive areas of the head and neck region.

ACKNOWLEDGEMENTS

REFERENCES

1 Cakir BO, Adamson P, Cingi C. Epidemiology and economic burden of nonmelanoma skin cancer. *Facial Plastic Surgery Clinics of North America* 2012; **20**:419-22.

2 Kim RH, Armstrong AW. Nonmelanoma skin cancer. *Dermatol Clin* 2012; **30**:125-39.

3 Levell NJ, Igali L, Wright KA, Greenberg DC. Basal cell carcinoma epidemiology in the UK: the elephant in the room. *Clinical & Experimental Dermatology* 2013; **38**:367-9.

4 Holm A, Nissen CV, Wulf HC. Basal Cell Carcinoma is as Common as the Sum of all Other Cancers: Implications for Treatment Capacity. *Acta Derm Venereol* 2016; **96**:505-9.

5 Deady S, Sharp L, Comber H. Increasing skin cancer incidence in young, affluent, urban populations: a challenge for prevention. *Br J Dermatol* 2014; **171**:324-31.

6 Crowson AN. Basal cell carcinoma: biology, morphology and clinical implications. *Modern Pathology* 2006; **19**:127.

7 Cohen PR, Schulze KE, Nelson BR. Basal cell carcinoma with mixed histology: a possible pathogenesis for recurrent skin cancer. *Dermatologic Surgery* 2006; **32**:542-51.

8 Kamyab-Hesari K, Seirafi H, Naraghi ZS, et al. Diagnostic accuracy of punch biopsy in subtyping basal cell carcinoma. *Journal of the European Academy of Dermatology & Venereology* 2014; **28**:250-3.

9 Trakatelli M, Morton C, Nagore E, et al. Update of the European guidelines for basal cell carcinoma management. *European Journal of Dermatology* 2014; **24**:312-29.

10 Burdon-Jones D, Thomas PW. One-fifth of basal cell carcinomas have a morphoeic or partly morphoeic histology: implications for treatment. *Australas J Dermatol* 2006; **47**:102-5.

11 Wolberink EA, Pasch MC, Zeiler M, et al. High discordance between punch biopsy and excision in establishing basal cell carcinoma subtype: analysis of 500 cases. *Journal of the European Academy of Dermatology & Venereology* 2013; **27**:985-9.

12 Richmond-Sinclair NM, Pandeya N, Ware RS, et al. Incidence of basal cell carcinoma multiplicity and detailed anatomic distribution: longitudinal study of an Australian population. *J Invest Dermatol* 2009; **129**:323-8.

13 Betti R, Radaelli G, Mussino F, et al. Anatomic location and histopathologic subtype of basal cell carcinomas in adults younger than 40 or 90 and older: any difference?. *Dermatologic Surgery* 2009; **35**:201-6.

14 Lu G, Fei B. Medical hyperspectral imaging: a review. *J Biomed Opt* 2014; **19**:10901.

15 Neittaanmaki-Perttu N, Gronroos M, Jeskanen L, et al. Delineating margins of lentigo maligna using a hyperspectral imaging system. *Acta Derm Venereol* 2015; **95**:549-52.

16 Neittaanmaki-Perttu N, Gronroos M, Tani T, et al. Detecting field cancerization using a hyperspectral imaging system. *Lasers in Surgery & Medicine* 2013; **45**:410-7.

17 Que SKT. Research Techniques Made Simple: Noninvasive Imaging Technologies for the Delineation of Basal Cell Carcinomas. *J Invest Dermatol* 2016; **136**:33.

18 Larson B, Abeytunge S, Seltzer E, et al. Detection of skin cancer margins in Mohs excisions with high-speed strip mosaicing confocal microscopy: a feasibility study. *Br J Dermatol* 2013; **169**:922-6.

19 Cheng HM, Guitera P. Systematic review of optical coherence tomography usage in the diagnosis and management of basal cell carcinoma. *Br J Dermatol* 2015; **173**:1371-80.

20 Venturini M, Gualdi G, Zanca A, et al. A new approach for presurgical margin assessment by reflectance confocal microscopy of basal cell carcinoma. *Br J Dermatol* 2016; **174**:380-5.

21 Wang KX, Meekings A, Fluhr JW, et al. Optical coherence tomography-based optimization of mohs micrographic surgery of Basal cell carcinoma: a pilot study. *Dermatologic Surgery* 2013; **39**:627-33.

22 Nassiri-Kashani M, Sadr B, Fanian F, et al. Pre-operative assessment of basal cell carcinoma dimensions using high frequency ultrasonography and its correlation with histopathology. *Skin Research & Technology* 2013; **19**:132.

23 Jambusaria-Pahlajani A, Schmults CD, Miller CJ, et al. Test characteristics of high-resolution ultrasound in the preoperative assessment of margins of basal cell and squamous cell carcinoma in patients undergoing Mohs micrographic surgery. *Dermatologic Surgery* 2009; **35**:9-15.

24 Bobadilla F, Wortsman X, Munoz C, et al. Pre-surgical high resolution ultrasound of facial basal cell carcinoma: correlation with histology. *Cancer Imaging* 2008; **8**:163-72.

25 Wetzig T, Kendler M, Maschke J, et al. No clinical benefit of preoperative fluorescence diagnosis of basal cell carcinoma localized in the H-zone of the face. *Br J Dermatol* 2010; **162**:1370-6.

26 Stenquist B, Ericson MB, Strandeberg C, et al. Bispectral fluorescence imaging of aggressive basal cell carcinoma combined with histopathological mapping: a preliminary study indicating a possible adjunct to Mohs micrographic surgery. *Br J Dermatol* 2006; **154**:305-9.

27 van Loo E, Mosterd K, Krekels GA, et al. Surgical excision versus Mohs' micrographic surgery for basal cell carcinoma of the face: A randomised clinical trial with 10 year follow-up. *Eur J Cancer* 2014; **50**:3011-20.

28 Gulleth Y, Goldberg N, Silverman RP, Gastman BR. What is the best surgical margin for a Basal cell carcinoma: a meta-analysis of the literature. *Plastic & Reconstructive Surgery* 2010; **126**:1222-31.

29 Saari H, Aallos V, Holmlund C, et al. Handheld hyperspectral imager. *Next-Generation Spectroscopic Technologies III* 2010/04/28; **7680**:76800D.

30 Jacques SL. Optical properties of biological tissues: a review. *Physics in Medicine & Biology* 2013; **58**:37.

31 Nascimento JMP, Dias JMB. Vertex component analysis: A fast algorithm to unmix hyperspectral data. *IEEE Trans Geosci Remote Sens* 2005; **43**:898-910.

32 Bowles JH, Palmadesso PJ, Antoniades JA, et al. Use of filter vectors in hyperspectral data analysis. *Proceedings of SPIE - The International Society for Optical Engineering* 1995; **2553**:148-157.

33 Barnes RJ, Dhanoa MS, Lister SJ. Standard Normal Variate Transformation and De-Trending of Near-Infrared Diffuse Reflectance Spectra: *Applied Spectroscopy* 1989; **43**:772-7.
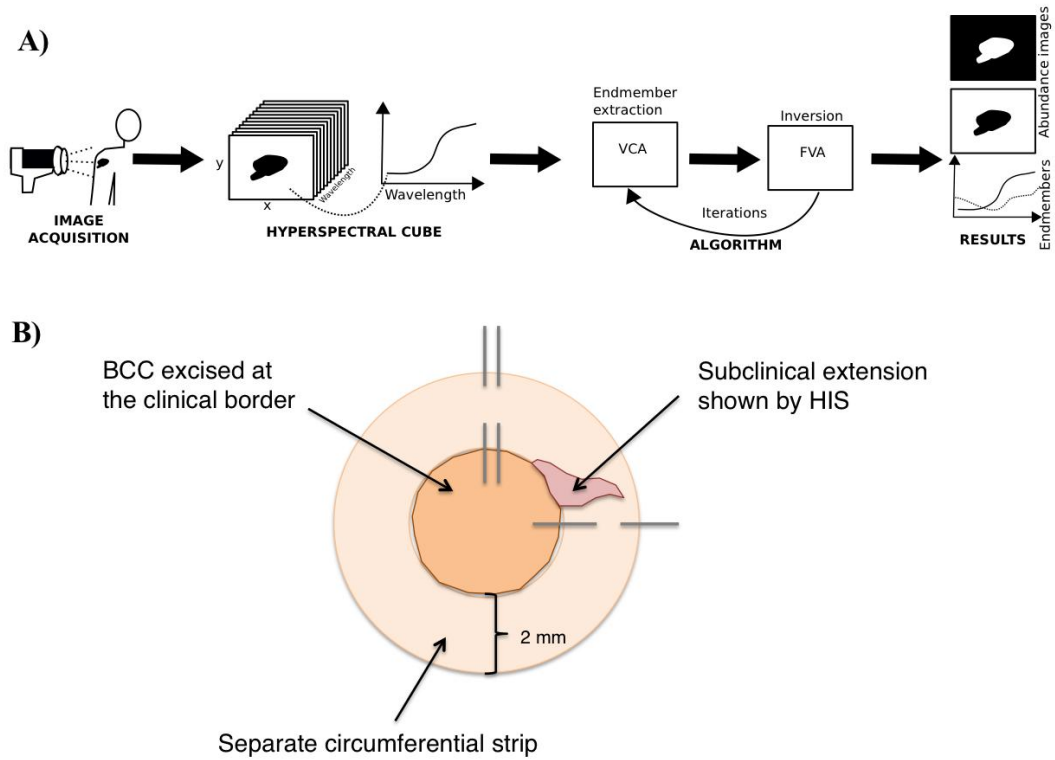
FIGURES AND LEGENDS

Fig. 1 A) Hyperspectral imaging process and B) operation technique to verify the subclinical extension detected by HIS.
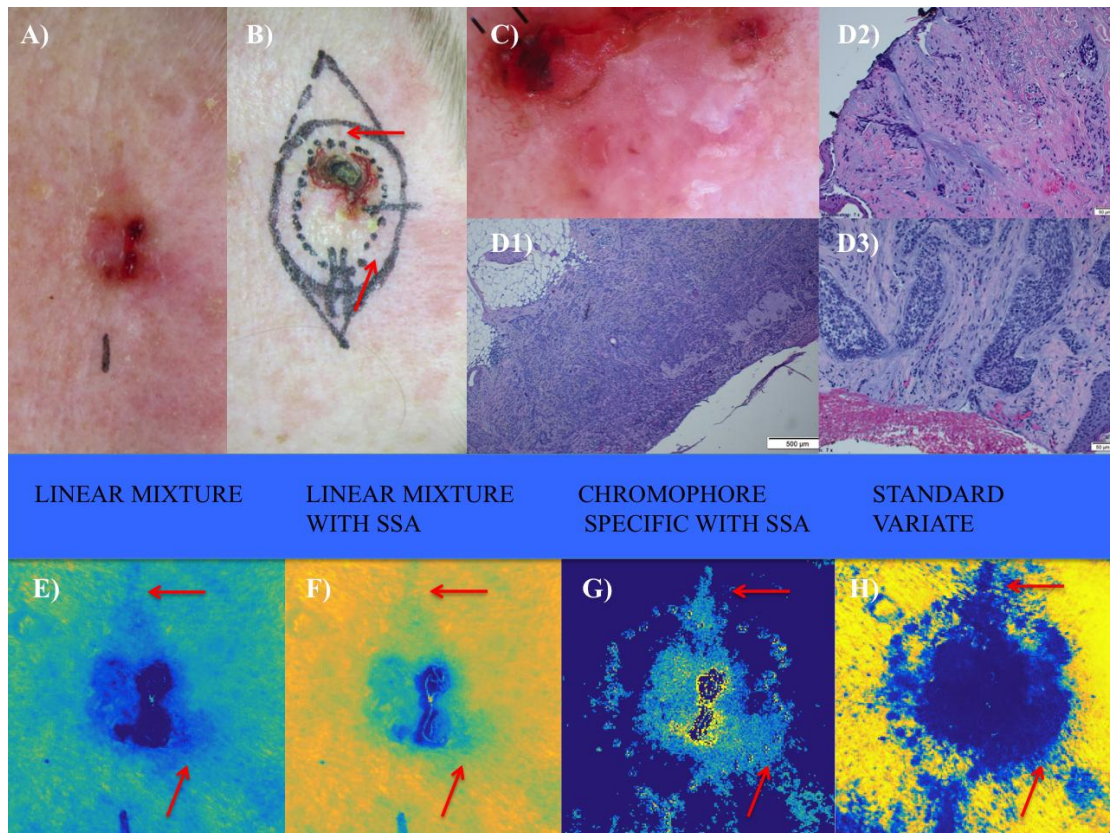
Fig. 2 Example patient with BCC delineated wider by HIS. Histologically, there was a nodular, superficial, micronodular, and infiltrative BCC, with perineural invasion, which showed subclinical micronodular growth in the marginal strip shown by HIS (arrows). A) Clinical picture, B) final excision with our operation technique, C) dermatoscopy image, D1) histological image from the main tumour area with the different aggressive growth patterns D2–D3) histological image, where the subclinical extension of BCC was detected in the separate marginal strip (D2 lower arrow and D3 upper arrow). HIS abundance maps marking the clinically and dermatoscopically assessed tumour border on the skin (arrows pointing the subclinical extension detected by HIS): E) linear mixture F) linear mixture with single scattering albedo (SSA), G) chromophore specific with SSA H) standard variate.

TABLES

Table 1. Histopathological analyses of the BCCs, anatomic location of the lesion, interpretation of the mathematical models, and the HIS outcome compared to clinical evaluation.

esion	Anatomic location of the lesion	BCC subtype in the biopsies	BCC subtype in the final excision	BCC subtype in the separate circumferential strip	Additional histopathological findings	Linear mixture model	Enhanced linear mixture model	Chromo-phore specific model	Mean value model	HIS outcome compared to the clinical assessment, and confirmed histologically
1	right cheek		superficial, nodular, micronodular		sun damaged skin	+	+	+	+	false pos.*
2	tip of nose		superficial, nodular		sun damaged skin	-	-	-	0	smaller**
3	preaurically on right cheek	nodulocystic	superficial, nodular, micronodular	superficial	solar lentigo	+	+	+	+	wider***
4	tip of nose		superficial, nodular, micronodular, infiltrative, basosquamous		sun damaged skin	-	-	-	0	smaller
5	lateral to nasolabial fold on right cheek	nodular	nodular		sun damaged skin	-	-	-	-	smaller
6	left cheek	nodular, micronodular	nodular, micronodular		sun damaged skin	-	-	-	-	smaller
7	forehead	nodular, micronodular	superficial, nodular, micronodular, infiltrative with perineural invasion	micronodular	actinic keratoses	+	+	+	+	wider
8	left auricle	superficial, nodular	superficial, nodular		sun damaged skin	-	-	-	0	smaller
9	right temple	nodular, micronodular, sclerotic	nodular, micronodular, infiltrative with perineural invasion	micronodular	solar lentigo	+	+	+	0	wider
10	left auricle	superficial, nodular	nodular, micronodular, infiltrative	micronodular	sun damaged skin	=	=	=	0	false neg. ****
11	neck, behind left ear		nodular		actinic kertoses, solar lentigo	-	-	-	-	smaller
12	left cheek	nodular	superficial, nodular		sun damaged skin, solar lentigo	+	+	+	+	false pos.
13	left cheek	nodular	cicatrix		eczema	-	-	-	-	smaller

14	right ala of nose	nodular	nodular, micronodular	nodular, micronodular	actinic keratoses	=	=	=	=	false neg.
15	right temple	superficial	superficial, nodular, micronodular, infiltrative with perineural invasion		sun damaged skin, ulcer	-	-	-	-	smaller
16	forehead	nodular, infiltrative	nodular, micronodular	nodular, micronodular	sun damaged skin	0	+	+	+	wider

(+) interpret wider in the abundance maps

(-) interpret smaller in the abundance maps

(0) too much of artefact for interpretation

(=) interpreted as same borders as ~~than~~ visually assessed (the margins announced in the tumor specimen were from 0 to 0,9 mm)

* HIS delineated the lesion wider than clinical assessment, but this wasn't supported by histopathology

** HIS delineated the lesion smaller than clinical assessment, and histopathology supported this

*** HIS delineated the lesion wider than the clinical assessment, and the histopathology supported this

**** HIS showed no suspicious for subclinical extension, but in the histopathology there was BCC in the circumferential strip

Appendix S1: Summarised description of the hyperspectral imaging system and the mathematical models

The studied handheld hyperspectral camera (VTT FPI VIS-VNIR Spectral Camera) was developed with the VTT Technical Research Centre of Finland; it is introduced in detail by Saari et al.[29] The camera uses visible-to-near infrared light (wavelengths 500–900 nm) based on a piezoactuated Fabry-Perot interferometer (FPI) with an adjustable air gap, one or two CMOS RGB colour sensors (MT009V022), basic camera objectives, microscope lenses, filters, and a dichroic beam splitter, which divides the light beam coming from the camera's light source (ring light around the lens system, a halogen based fibre-optic illuminator; Dolan-Jenner Fibre-Lite DC 950) into visible light and very near infrared light.

The FPI consists of reflecting mirrors in a cavity, and the air gap between these mirrors is adjustable. By tuning this air gap, it is possible to record different wavelengths[29]. The FPI reflects three wavelength peaks at one air gap width, and by changing the width of the gap, it is possible to record another set of three different wavelengths[29]. Changing the air gap width takes < 2 ms[29]. Thus, it is possible to receive spectral information at 70 different wavelengths very quickly.

At the same time as the spectral information is gathered, the camera records a traditional 2D image with a resolution of 240x320 pixels, which are approx. 125 μm in width. Every pixel has a unique spectral graph that forms the third dimension of the spectral data cube (see *Fig. 1A*). Use of this data cube enables spectral mapping, i.e. the localisation of the spectral information in the imaged area. With the 500–900 nm

wavelengths, it is possible to reach approx. up to 2 mm penetration depth, with shorter wavelengths reaching more superficial depths and the wider wavelengths penetrating the deeper parts of the skin.

The part of the camera system touching the object (i.e. the patient's skin) is a dark cover tube that is available in varying sizes (range 2.5–12 cm^2). The tube removes background light and defines the field of view (FOV). The maximum FOV is thus 12 cm^2. The cover tubes are selected according to the size of the lesion, and smaller tubes enable the flattening of uneven surfaces, such as the nose or ear.

The spectral data cube – i.e. the recorded reflectance gathered by the colour sensors in the ENVI standard data format – is transferred to a computer via a USB2 port[29]. The different wavelengths are recorded in the different proportions of the RGB sensor output. This data is converted to reflectance X, in which $X_\lambda = (I_\lambda - I_{dark}) / (I_{\lambda,white} - I_{dark})$, where λ is all recorded wavelengths, I_λ is the recorded raw digital image, $I_{\lambda,white}$ is the recorded white reference, and I_{dark} is the dark current of the colour sensor.

The huge amount of information imaged in the spectral cube can be represented numerically, and thereafter, it is possible to apply an algorithm, i.e. a mathematical model with computational calculations. With the mathematical modelling, it is possible to calculate an end-member (i.e. pure spectrum) from the spectral graphs of every pixel in the image (see *Fig. 1A)*. These end-members are converted for interpretation to abundance maps, which show the localisation of the end-member spectra in the image. Every mathematical model is an assumption of the real world, and by these assumptions, we are able to visualise the information on the spectral dimension of the data cube.

Our mathematical models used the information on tissue optical properties and the coefficients of different parameters available in the literature[30]. The main properties affecting the tissue optics and reflectance are absorption and scattering. Both absorption and scattering vary based on the chromophores (i.e. melanin, water, haemoglobin, etc.) in different tissues[30]. Interestingly, it is possible to numerically represent the three layers of the skin (epidermis, dermis, and subcutaneous fat) as a combination of the absorption and scattering properties of the different chromophores[30].

The four numerical methods used in this study were 1) an inversion of the linear mixture model using iterative Vertex Component Analysis – i.e. the linear mixture, 2) an inversion of the linear mixture model from the estimated single scattering albedo (SSA) using iterative Vertex Component Analysis – i.e. the linear mixture with SSA, 3) a closed form chromophore-specific approximation for the estimated SSA – i.e. chromophore specific with SSA, and 4) a modified standard normal variate correction algorithm – i.e. a standard variate.

1) Linear mixture

The linear mixture algorithm assumes that the spectra in the imaged cube are a linear mixture of some limited number of characterised spectra, which are named end-members. The linear mixture of end-members can be expressed in matrix form following $X = MY$, where X is the recorded spectral data, M is the mixing matrix, and Y are the end-members. The linear mixture model uses vertex component analysis (VCA) [31] to define the end-members. The mixing matrix describes proportion of end-members in every pixel. To calculate computationally the inversion of the mixing matrix, filter vector analysis (FVA) [32] was used. Next, M and Y are solved. This step is

iteratively repeated several times to determine the right number of end-members. Selection of the right number of end-members is arrived at in order to minimise $\min_{k}\|X - \hat{X}\|_{FRO}$, where k is the number of end-members, which usually varies between 2 and 6 because VCA usually detects 2–4 end-members on the skin with malignancy based on experience. With this model, we assume the end-members of the healthy skin and tumour area differ from each other.

2) Linear mixture with SSA

The skin's reflectance spectra is not actually linearly mixed. The reflectance of the skin is actually a non-linear mixture of the different chromophores' absorbance and scattering properties. With a rough estimate, the reflectance spectra can be converted into a single scattering albedo (SSA). SSA is calculated based on the scattering coefficient and total absorption coefficient. SSAs are linearly mixed. After this conversion, we apply VCA[31] to define the end-members. Thus, the non-linear "real world" is converted to a more linear form, enabling the use of VCA. With this model, we assume that the calculated end-members of the healthy skin and the tumour area might more accurately represent the "real world".

3) Chromophore specific with SSA

In this model, SSA is used to describe the recorded reflectance upon which FVA[32] is applied to solve the different proportion of chromophores. The coefficients of different chromophores are multiplied by the proportion of the chromophores. Thus, we create reconstructed data, in which we can weigh a certain chromophore's end-member in the abundance map. In doing so, we assume that the proportion of certain chromophores differs in the healthy skin and the tumour area. In the chromophore-specific model, we produce the maps with oxyhaemoglobin

concentration, deoxygenated haemoglobin concentration, total blood concentration, oxygen saturation, mean scattering of simulation, mean absorption of simulation, melanin concentration, and baseline concentration. For example, the tumour uses more oxygen, and in the abundance map of "deoxygenated haemoglobin concentration", we can see the difference the between the tumour area and the healthy skin. Thus, we are able to visualize a certain chromophore in the abundance map.

4) Standard variate

The standard variate model differs from the three models presented above. It has a statistical background, and in essence, it compares how the spectra differ from the mean spectra. The standard variate algorithm reduces spectral noise and eliminates the background effect[33]. This means that if there are many similar spectra in the imaged cube, the standard variate model will characterise the differences in the spectra without the homogenous background information. Originally, standard variate algorithm was developed for the single point spectroscopy. For our purpose we added some modifications so that it gives us mapping in spatial domain, which separates two areas from image, which refers to background (healthy tissue) and anomalous area (tumorous tissue).